1 # X-ray absorption, X-ray diffraction and electron microscopy

2 ## study of spent cobalt based catalyst in semi-commercial scale

3 ## Fischer-Tropsch synthesis

4

5 **Nikolaos E. Tsakoumis[a], Roya Dehghan-Niri[b], Magnus Rønning[a], John C.**

6 **Walmsley[b,d], Øyvind Borg[c], Erling Rytter[a,c], Anders Holmen[a]**

7

8 [a] Department of Chemical Engineering, Norwegian University of Science and Technology (NTNU),

9 NO-7491 Trondheim, Norway.

10 [b] Department of Physics, Norwegian University of Science and Technology (NTNU), NO-7491

11 Trondheim, Norway.

12 [c] Statoil RDI, Research Centre Trondheim, Postuttak, NO-7005 Trondheim, Norway.

13 [d] SINTEF Materials and Chemistry, NO-7465 Trondheim, Norway

14

15 Roya Dehghan-Niri current address: Statoil RDI, Research Centre Trondheim, Postuttak, NO-7005

16 Trondheim, Norway

17

18 **Corresponding author:** Nikolaos E. Tsakoumis, tsakoumi@chemeng.ntnu.no, Norwegian

19 University of Science and Technology (NTNU), Department of Chemical Engineering, Sem

20 Sælandsvei 4, NO-7491 Trondheim. Phone (office): +47 735 97018

21

22 **Abstract**

23 Calcined, reduced and spent $Co-Re/\gamma-Al_2O_3$ catalysts for Fischer – Tropsch synthesis (FTS)

24 were characterized and compared. Co-K-edge and $Re-L_{III}$-edge X-ray absorption near edge

25 structure (XANES), X-ray powder diffraction (XRPD), transmission electron microscopy

26 (TEM) and H_2 chemisorption were used to provide insight into structural transformations that

27 the catalyst experiences during a month of operation in a semi-commercial FTS plant.

28 Results from the core techniques for nanoparticle size determination suggest that sintering of

29 the cobalt crystallites is one important deactivation mechanism in FTS performed in slurry

30 reactors. In addition, a higher degree of reduction is observed for the spent catalytic material,

31 while Re appears in a partially reduced state before and after reaction. The particle size

32 distribution together with the spread of Co nanoparticles on the $\gamma-Al_2O_3$ surface indicates

33 crystallite migration as the prevailing mechanism.

34

1. Introduction

The Gas-to-liquid (GTL) process is the conversion of natural gas derived synthesis gas into hydrocarbons via Fischer – Tropsch synthesis (FTS) [1]. In recent years large investments have been made in the field of GTL with the Oryx and Pearl plants in Qatar to be the latest achievements. This dynamic growth is further supported by new technologies for exploiting unconventional gas sources that have allowed larger amounts of natural gas to reach the market. A higher gas supply might increase the price difference of crude oil and natural gas, which will likely trigger more research and applications in the area of GTL [2].

The currently commercialized GTL technologies use supported cobalt catalysts for the Fischer – Tropsch synthesis step, in which CO and H_2 are transformed to a wide range of linear long-chain hydrocarbons and water [3]. One of the challenges in applied Co-based FTS is the lifetime of the catalyst. Due to the relatively high price of cobalt, continuous operation without catalyst replacement for long periods is favourable and, therefore, a lot of effort has been made towards understanding catalyst deactivation [4] and regeneration phenomena [5]. The deactivation profile of Co-FTS is characterized by two regimes of different deactivation rate and degree of reversibility [6]. The partial reversibility of the activity loss during different time on stream upon mild H_2 treatments suggests that more than one deactivation mechanism contributes to the deactivation profile. Deactivation with irreversible character is of high industrial significance. Moreover, due to the narrow operational window of FTS and the correlation of conversion level and deactivation rate, which may lead to several deactivation pathways, investigation through accelerated deactivation tests is difficult. As a result of the slow development of such phenomena extended FTS runs lasting several weeks to months are required and hence the detailed study of FTS deactivation in the long term dictates collaboration between industry and academia.

Although GTL today can be regarded as proven technology there is a lack of information on long term deactivation and one should go back in time to find information on the industrial scale [7]. The number of publications and reports dealing with characterization of catalysts used in extended FTS trials (>500 h) is limited. Published information suggests that sintering of cobalt particles [8–10], formation of inactive cobalt-support mixed phases [10,11] and formation of stable carbon species [12–15] can be the main cause of the "irreversible" catalyst deactivation in FTS.

In the present study a spent catalyst operated in a semi-commercial demonstration GTL unit with production capacity of 1000 bpd [16] was analysed and compared to its fresh analogue. The Co-Re/γ-Al$_2$O$_3$ catalyst sample was unloaded from the slurry reactor after a month of operation at commercial FTS conditions. Ex situ and quasi in situ characterization techniques were employed in order to reveal changes that occurred during operation and assist towards the understanding of the deactivation mechanism at the industrial scale.

2. Experimental

2.1. Catalyst preparation

The nominal composition of prepared catalysts for laboratory use was 20 wt.% Co and 0.5 wt.% Re supported on γ-Al_2O_3. These catalysts were prepared by one-step aqueous incipient wetness co-impregnation of $Co(NO_3)_2 \cdot 6H_2O$ and $HReO_4$. The support was a Puralox SCCa type material from Sasol GmbH. The laboratory catalysts are dried in air at 393 K for 3 hours and calcined in air at 573 K for 16 hours before use. The commercial catalyst investigated in this study was prepared similarly by adapting the laboratory procedure to the use of large scale production equipment. The present study deals with the characterization of the industrial catalyst in different steps of activation and operation; the freshly calcined catalyst (Cat), a reduced catalyst embedded in FT-wax (Cat-R-W) and a spent catalyst (Cat-R-W-FT). The materials were characterised as received and at different stages of the applied post-treatments, i.e. de-waxing and temperature programmed hydrogenation (TPH). All catalysts were provided by Statoil Petroleum AS.

2.2. Hydrogen Chemisorption

Hydrogen adsorption isotherms were recorded on a Micromeritics ASAP 2020 unit at 313 K. The samples (0.2 g) were initially treated with He at 393 K for 2h. Consequently, it was evacuated at 313 K for 1 h, and then reduced in flowing hydrogen at 623 K for 10 h. The temperature was increased at 3 K/min from 313 to 623 K. After reduction, the sample was evacuated for 1 h at 603 K and for 30 min at 373 K before subsequent cooling to 313 K. The adsorption isotherm was recorded at this temperature and was extrapolated to zero pressure where the amount of chemisorbed hydrogen was determined. Furthermore, in order to calculate the dispersion, it was assumed that two cobalt sites are covered by one hydrogen molecule [17] and that rhenium does not contribute to the amount of hydrogen adsorbed. The average diameter of metallic cobalt nanoparticles ($d(Co^0)$, nm) was calculated from the cobalt metal dispersion (D, %) by assuming uniform spherical metal particles (site density of 14.6 at/nm^2).

2.3. Transmission electron microscopy

TEM experiments were performed with a JEOL 2010F equipped with a field emission gun, operating at 200 kV accelerating voltage. TEM samples were prepared by dispersion of the crushed catalysts powder on a carbon supported Cu mesh grid. In order to identify different phases in the samples, both diffraction and high resolution TEM (HRTEM) were applied. Particle size measurements were performed by direct measurements on the TEM images using the Digital Micrograph tools.

2.4. X-ray Absorption Near Edge Structure

The BM01B station of the Swiss-Norwegian beam lines (SNBL) at the European Synchrotron Radiation Facility (ESRF) was used for the X-ray absorption experiments [18]. XANES spectra were recorded at the Co K-edge (E = 7709 eV) and Re L_{III}-edge (E = 10535.3 eV) using a double crystal Si (111) monochromator. The data collection was carried out in transmission mode. Ion chamber detectors filled with mixtures of inert gases at ambient temperature and pressure were used for measuring the intensities of the incident (I_0) and transmitted (I_t) X-rays. The energy calibration has been done by measuring the spectrum of Co and Re foils. The definition of edge energy was done by taking the observed maximum of the first derivative. Linear combination analysis (LCA) of the XANES spectra obtained from reference materials including Co foil, Co_3O_4, CoO and $CoAl_2O_4$ provide quantified information on the concentration of different phases. Linear combination analysis (LCA) was performed by Athena software, part of the Horae software package (Version 1.2.9) [19].

For the XANES experiments the *in situ* cell that was used was developed based on previously proposed configurations [20,21]. The detailed design of the cell and description of the experimental set-up can be found elsewhere [22]. In brief a quartz capillary is used as a plug flow reaction cell. The capillary has overall length, outer diameter, and wall thickness of 60 mm, 1 mm, and 0.02 mm, respectively. It is inserted into a stainless steel bracket and glued on its frame. Swagelock fittings are used to connect the bracket with the basic construction of the cell. The catalyst bed is immobilized by quartz wool plugs and lying above a vertical hot air blower. The reactor inlet and outlet are heated up to 423 K by heating cartridges. The chosen cell configuration can accommodate the combination of several X-ray based characterization techniques at industrially relevant conditions [23].

2.5. X-ray powder diffraction

The catalyst was characterized by X-ray powder diffraction (XRPD). The measurements were performed at the BM01A station of the SNBL. In the BM01A station a square X-ray beam of 500 μm was adjusted to a corresponding wavelength of 0.6978 Å. Powder diffraction patterns were collected using a mar345 area detector with a diameter of 345 mm at a sample-to-detector distance of 230 mm. The sample was inserted into a quartz capillary prior analysis. Quartz capillaries of 0.7 mm in diameter were used for minimizing instrumental broadening [24]. The exposure time was 45 seconds and the obtained images were converted to normal one-dimensional powder patterns using the program FIT2D [25]. Pawley fit of the obtained data sets was applied with fityk [26] and Topas v 4.2 software [27].

The *in situ* cell used for the XRPD experiments was based in the design described by Norby [28]. The principle of the cell construction is similar to the one used for the XANES experimentation. In addition one end of the basic construction of the cell can be attached to a

goniometer allowing semi-rotating/swinging mode for improved statistics of the recorded pattern. The description of the experimental set-up can be found elsewhere [29].

2.6. Wax extraction (De-waxing)

Wax extraction has been done using a Soxhlet extractor and by using tetrahydrofuran (THF) solvent. Initially the solvent was degassed overnight under the flow of Ar (99.999 %) in order to remove dissolved O_2. Subsequently the system was heated to 358 K and left overnight to complete several reflux cycles under Ar atmosphere. Finally the part of the Sohxlet apparatus containing the catalyst was isolated and transferred to a glove-box where the catalyst was unloaded and stored in Schlenk type flasks. The flasks where evacuated for 2 h in order to remove the remaining THF. The wax extraction procedure resulted in a passivated catalyst.

2.7. Temperature Programmed Hydrogenation

Certain catalysts were treated with H_2 at elevated temperature. The Temperature Programmed Hydrogenation (TPH) treatment has been done under 2.5 ml/min pure H_2 (99.999 %) flow at ambient pressure. Less than 8 mg of the sample was loaded into the quartz capillary and stabilized by quartz wool plugs. The sample was heated from ambient temperature to 673 K at a rate of 3 K/min. When the desired set point was reached, the temperature was held for 4 h before switching to a He flow of 5 ml/min and ramp down to room temperature. The TPH protocol was identical for all the catalytic samples and for all the applied X-ray based techniques.

2.8. Fischer-Tropsch Synthesis

Fischer-Tropsch synthesis was carried out in a semi-commercial demonstration GTL plant at Mossel Bay, South Africa, integrated with an existing GTL production facility. The syngas available was produced by combined reforming with a composition adapted to an iron catalyst in high-temperature Fischer-Tropsch synthesis. Before entering the semi-commercial plant, the H_2/CO ratio of the syngas was adjusted to ca. 2.0 or less by removing some hydrogen through a membrane, to suit the requirements of the cobalt based process. The preheated and purified syngas entered the pressurized slurry bubble column reactor containing fine particles of the cobalt based catalyst dispersed in molten wax. The typical operating temperature was 210-240 °C. A description of the unit can be found elsewhere [16].

3. Results

The catalyst was characterised at different stages of its lifetime and after de-waxing and hydrogenation post-treatments by XANES, XRPD, TEM and H_2 chemisorption.

Table **1** summarises the post-treatments that were applied to the samples and the type of data obtained from each sample.

The calcined catalyst (Cat) was reduced and embedded in wax (Cat-R-W) to preserve it in the reduced state. The catalyst was added into the semi-commercial scale bubble column reactor of 2.7 m in diameter and performed Fischer – Tropsch synthesis for several weeks (Cat-R-W-FT). These three main materials were analysed systematically before and while been subjected to post-treatments. In particular Cat-R-W and Cat-R-W-FT were exposed to a de-waxing procedure, while for catalytic materials Cat, Cat-R-W-D and Cat-R-W-FT-D a temperature programmed protocol was applied under H_2 atmosphere.

Table 1: Catalyst treatments and analysis.

Sample name	Co-XANES	Re-XANES	XRPD	TEM	H_2 - chemisorption
Cat	X		X		X
Cat-TPH	X		X		
Cat-R-W	X	X	X		
Cat-R-W-D	X		X	X	
Cat-R-W-D-TPH	X		X		
Cat-R-W-FT	X	X	X		
Cat-R-W-FT-D	X		X	X	X
Cat-R-W-FT-D-TPH			X		

R = reduction, W = waxing, D = de-waxing, TPH = Temperature programmed hydrogenation, FT = Fischer – Tropsch
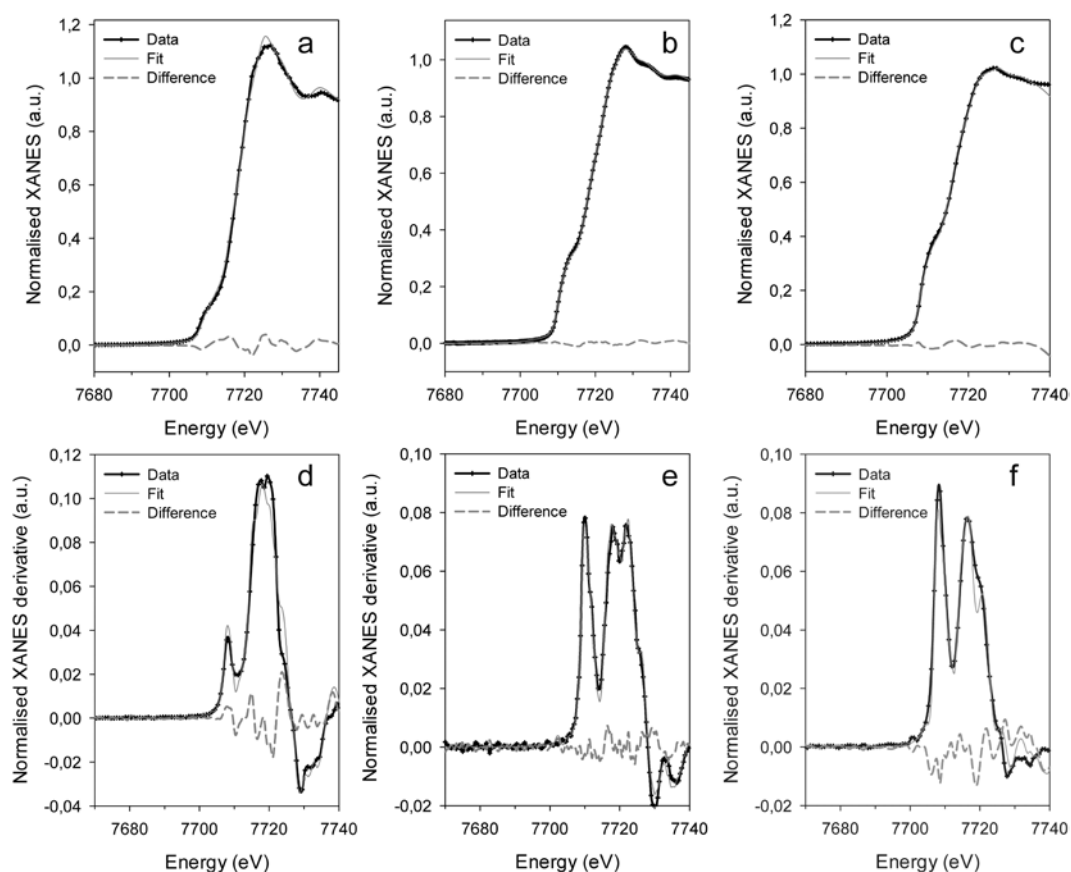
3.1. X-ray Absorption Near Edge Structure at the Co-K-edge

Cobalt XANES at the K-edge was performed on the samples at different stages of catalyst lifetime. Spectra of the calcined catalyst (Cat) resemble the Co_3O_4 standard. The wax embedded reduced catalyst (Cat-R-W) was measured ex situ. The results indicate that the reduced catalyst embedded in FT-wax was partially re-oxidized, having a degree of reduction (DOR) of 38%, most probably due to oxidation from air during storage. A white line feature that is present in all cobalt oxides is evident in the obtained spectra (Figure 1). Linear combination analysis of reference spectra suggested that the CoO phase is dominating, while small amounts of $CoAl_2O_4$ may also exist (Table 2).

Figure 1. XANES spectra, their first derivatives together with the fit from linear combination of reference spectra. From left to right (a,d) Cat-R-W (b,e) Cat-R-W-D catalyst after TPH treatment and (c,f) Cat-R-W-FT catalyst.

The catalyst was de-waxed, treated with H_2 and characterised during the in situ treatment. In particular the Cat-R-W-D catalyst was loaded into a quartz capillary and treated at temperature programmed hydrogenation conditions (3 K/min to 673 K at 2.5 ml/min H_2). Initially the catalyst Cat-R-W-D contained mainly the oxide phases CoO and Co_3O_4 possibly formed during the de-waxing procedure. A metallic core is also assumed to co-exist since the sample responded to an externally applied magnetic field. However, linear combination analysis of XANES spectra shows that the fraction of metallic Co to be less than 10%. The following TPH treatment initially converts the Co_3O_4 into CoO which is eventually transformed to metallic cobalt. At 673 K the degree of reduction of the catalyst reached 72 %. The evolution of the phases together with the obtained spectra is shown in Figure 2.

Table 2: Quantitative XANES results of the Co-Re/γ-Al₂O₃ catalyst after various treatments, obtained by LC analysis of the XANES spectra of reference materials.

Catalyst Samples	Co⁰ (%)	CoO (%)	Co₃O₄ (%)	CoAl₂O₄ (%)
Cat-R-W	38	52	7	3
Cat-R-W-D-TPH	72	23	-	5
Cat-R-W-FT	80	17	-	3
Cat-R-W-FT-D	26	63	10	-

Error +/- 5%

A slice of spent catalyst Cat-R-W-FT was analysed protected in kapton tape, wrapped inside a N_2 flushed glove-box. The metallic Co content of the Cat-R-W-FT sample was 80%. The shape of the spectra of the spent sample strongly resembles metallic cobalt lacking any pre-edge or white line characteristics, Figure 1. From the LCA of XANES spectra a higher degree of reduction for the spent catalyst was calculated. In agreement with previous observations [30] cobalt – aluminates were detected in all the catalysts in similar levels, yet in concentrations falling inside the uncertainty of the technique [31]. Quantitative results are summarized in Table 2.
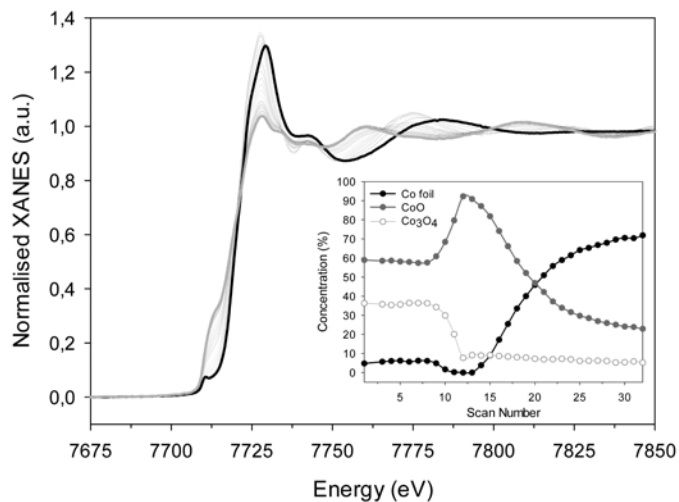
Figure 2. Obtained spectra from Cat-R-W-D during TPH treatment and phase concentration from XANES-LCA (insert). Thicker lines denote XANES spectra at room temperature (black) and at the end of the TPH treatment, 673 K (grey).

3.2. X-ray Absorption Near Edge Structure at Re-L$_{III}$-edge

XANES spectra at the Rhenium L$_{III}$-edge were acquired from the Cat-R-W and Cat-R-W-FT samples. The data were obtained ex situ and have lower signal to noise ratio as a result of the low levels of Re in the sample. Due to the plethora of Re oxidation states quantitative analysis through the linear combination of reference materials was not possible and an estimation of the state of Re has been made by the evaluation of edge position (defined here

as the maximum of the first peak at the first derivative) as previously performed [32,33]. Additionally the existence of particular features that are present in the spectra can be assessed.
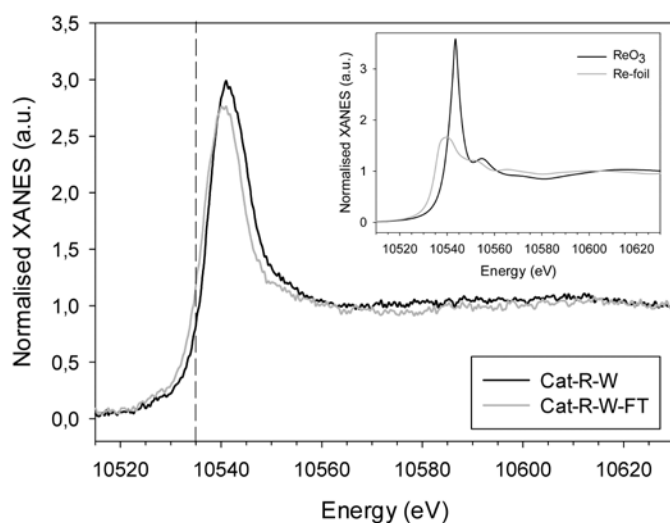

Figure 3. Re L$_{III}$-XANES spectra obtained from Cat-R-W, the spent catalyst Cat-R-W-FT and standards (Re-foil and ReO$_3$). Edge position is denoted with a dashed line.

Results reveal that the degree of reduction of Re in both the reduced wax embedded (Cat-R-W) and the spent catalyst (Cat-R-W-FT) is similar. From the maximum of XANES derivatives Re L$_{III}$-edge shifts of +2 eV and +1.7 eV are observed for the reduced and spent catalysts, respectively. The edge position for both samples suggests partially reduced catalysts, since the values are approaching the value of metallic Re at 10535 eV. The "white line" is present in both samples, while it is lower for the catalyst after reaction (Cat-R-W-FT). An obvious reason may be that the re-oxidation, which was observed in the spectra obtained at the Co k-edge and dealt with in the previous paragraph (§ 3.1), has affected rhenium as well. Although the edge energy is shifted towards low oxidation states the white line remains surprisingly intense. This has been previously attributed to the cationic character of rhenium existing in reduced Re/γ-Al$_2$O$_3$ catalysts, possibly due to interaction (electron transfer) of Re with the support [34–36]. Additionally the intensity of the resonance observed in the Re foil at approximately +20 eV is absent in the samples. A correlation between Re cluster size and intensity of the feature at 10553 eV has been previously demonstrated by theoretical XANES calculations [34]. The lack of the feature can be attributed to Re clusters with less than 10 atoms or even atomically distributed Re. Similar investigations on analogous FTS Co-Re bimetallic catalysts at the K and L$_{III}$ edges have shown a high possibility of Re being atomically distributed in the catalytic material and predominantly in contact with cobalt [33].

1   3.3. X-ray powder diffraction

2   X-ray powder diffraction (XRPD) patterns were obtained at the different stages of the trial

3   and the applied post-treatments. Both ex situ and in situ experiments were performed for the

4   different catalytic materials. The three main investigated samples (Cat, Cat-R-W-D and Cat-

5   R-W-FT-D) were subjected to an in situ XRPD-TPH treatment. An identical TPH protocol was

6   used including a temperature elevation to 673 K with a rate of 3 K/min under pure H_2 and a 4

7   hour hold, for all the samples as previously described.
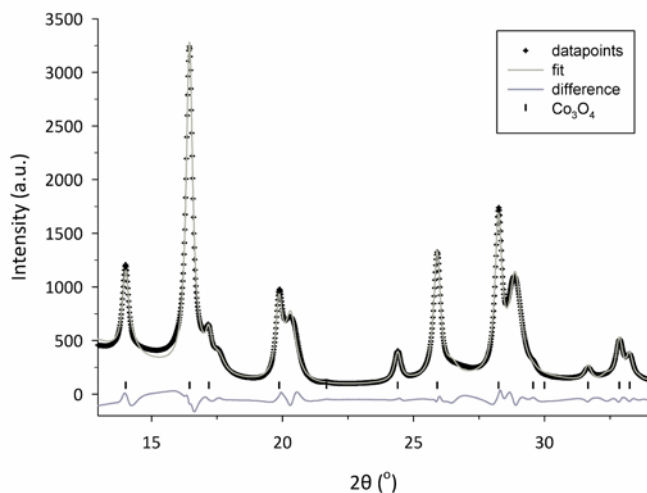
8

9   **Figure 4.** XRPD pattern of Cat consisting of Co_3O_4 crystallites dispersed on the γ-alumina support,

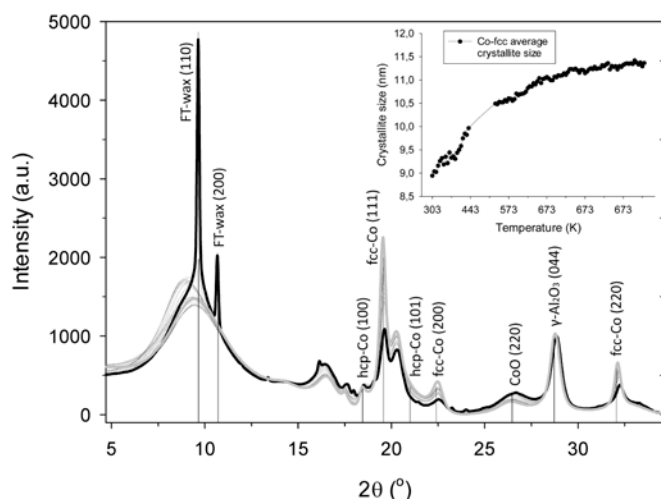10   plotted together with the calculated pattern and their difference.

11

12   The calcined catalyst (Cat) was inserted in the *in situ* cell and flushed with He for 1

13   hour. Diffraction patterns were acquired at room temperature. The pattern decomposition

14   showed that cobalt in the form of Co_3O_4 and γ-alumina are the only detectable crystalline

15   phases (Figure 4). Calculation of the Co_3O_4 crystallite size through the Scherrer equation

16   gave an average of 13.2 nm per crystallite. A corresponding size for the metallic cobalt

17   crystallites equal to 10.6 nm estimated from the expected volume decrease due to loss of

18   oxygen [37]. Throughout the *in situ* hydrogen treatment, X-ray diffraction patterns were

19   acquired by utilizing an area detector at the SNBL-BM01A station (Figure 5). XRPD results

20   confirm that the evolution of reduction is passing through the CoO reaction intermediate as

21   previously shown by in situ XANES [22]. The intensity versus time on stream, shown in

22   Figure 5, was obtained after normalising all the diffraction patterns to the intensity of the

23   (440) reflection of γ-alumina support. The use of the support as internal standard is based on

24   the fact that the lattice parameters and the line width obtained by the XRPD patterns are

25   identical before and after the reaction. The maximum reflections of the different crystalline

26   phases of cobalt including the (311) reflection from Co_3O_4, the (220) from CoO and the (111)

27   from fcc-Co were monitored. At the end of the TPH treatment the sample (Cat-TPH) contains

1 mainly γ-alumina and Co configured in the face centered cubic (fcc) crystal structure. A

2 broad peak is observed in the range where hcp Co reflections are expected. Similar

3 observations suggesting an intergrowth structure of fcc and hcp crystallites have been made

4 in the past in comparable Co-based supported catalysts for FTS [22,38]. The average cobalt

5 crystallite size was calculated from the full width at half maximum (FWHM) of the (111), (200)

6 and (220) reflections in the fcc-Co crystallites and found to be 7.9 nm after reduction at 673

7 K, significantly smaller than the estimate derived from the size of Co_3O_4.
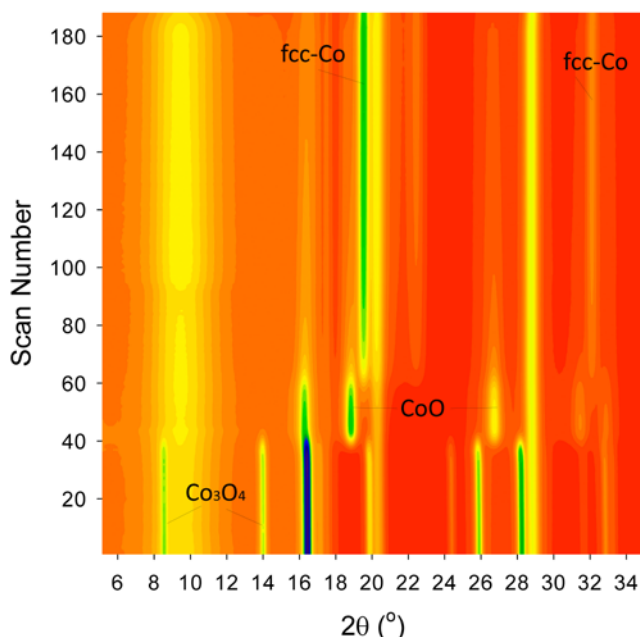
8

9 **Figure 5.** Intensity monitoring for the reflections (311) of Co_3O_4, (220) of CoO and (111) from fcc-Co
10 during catalyst reduction.

11

12 The de-waxed spent catalyst (Cat-R-W-FT-D) was subjected to an identical TPH

13 procedure. The obtained patterns were again normalised to the (440) reflection of the γ-Al_2O_3

14 (Figure 6). The initial diffraction pattern of the Cat-R-W-FT-D at room temperature shows the

15 sharp reflections of crystalline wax at low 2θ° angles (< 12°). This clearly demonstrates that

16 part of the wax remains even after the applied de-waxing procedure. During elevation of

17 temperature and above 313 K the FT-waxes melt and are transformed from solid to liquid

18 state. At 358 K no reflection from wax can be distinguished. The average crystallite size of

19 the fcc-Co phase was calculated before and after the TPH treatment at room temperature

20 and found to be 8.7 nm and 11.3 nm, respectively.

1

2 **Figure 6.** Diffraction patterns obtained during the TPH treatment of Cat-R-W-FT-D, together with the

3 average crystallite size calculated from the reflections of the fcc-Co (insert). Thicker lines denote

4 diffraction patterns at room temperature (black) and at the end of the TPH treatment, 673 K (grey).

5

6   A change in intensity of the cobalt and FT-wax reflections can be seen in Figure 7. It

7 appears that the actual reduction of the cobalt is taking place at around 443 K, were the

8 intensity of the (111) fcc-Co increases and the signal from the (220) CoO reflection

9 decreases. The FWHM of the fcc-Co reflections was followed and related to crystallite size

10 by the Scherrer equation, Figure 6. Initially, fluctuations in the calculated crystallite size were

11 observed that can be attributed to the elimination of the contribution from FT-wax in the

12 diffraction pattern resulting in a smoothening of the background and not to actual reduction of

13 the catalyst. An intensive narrowing of the peak was observed above 398 K (Figure 6). The

14 reflections in the broad area in the $2\theta^{\circ}$ range of the expected Co (101) hcp reflections were

15 also followed. Apparently, the formation of hcp-Co takes place simultaneously with the

16 formation of fcc-Co Figure 7. Similar growth of the crystallites of metallic Co have been

17 detected also in carbon supported catalysts [23].
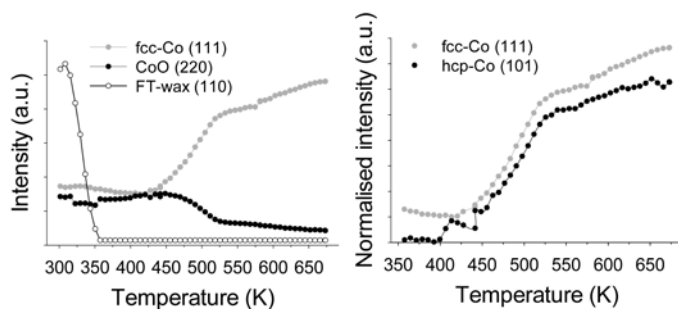
18

19 **Figure 7.** Intensity monitoring throughout TPH treatment of Cat-R-W-FT-D for (111) fcc-Co, (110) FT-

20 wax, (220) CoO and (101) hcp-Co. Note that the intensity of (101) hcp-Co reflection is multiplied by a

21 factor of 2.2 for comparison reasons.

22

1   By comparing the crystallite size obtained from the spent catalyst after the TPH procedure to
2   the one from the calcined catalyst after the H_2 treatment, a significant increase (43%) is
3   apparent suggesting that cobalt is going through a crystallite growth process with time on
4   stream. The difference is not clearly observable in the ex situ measurement of the spent
5   catalyst (Cat-R-W-FT) before the H_2 treatment and the reduced fresh catalyst (Cat-TPH), 9.3
6   nm and 7.9 respectively, where the crystallite size difference is not far from the accuracy of
7   the Scherrer equation. This observation can be attributed to surface oxidation and
8   passivation of the spent catalyst from slow oxygen diffusion through the wax, during sample
9   preparation for analysis. On a passivated surface, the contribution in the diffraction pattern
10   will rise only from the metallic core and will thus be underestimated. During exposure to H_2 at
11   elevated temperatures the oxide layer is reduced giving rise to signal from the whole of the
12   metallic particle. Additionally, the observed reflections of the CoO are further suppressed on
13   the Cat-R-W-FT-D-TPH catalyst, suggesting a higher degree of reduction for the spent
14   catalyst Figure 8. This is in accordance with observations of the DOR obtained by XANES-
15   LCA at the Co K edge. The quasi - in situ XRPD analysis of the catalytic samples clearly
16   demonstrates that the material has different properties in terms of crystallite size and degree
17   of reduction after its use in a semi-commercial scale unit. For further confirmation, in situ
18   XRPD monitoring of the Cat-R-W-D catalyst during TPH treatment was conducted and used
19   as reference (blank) experiment for clarifying any effect that the de-waxing procedure may
20   have had on the catalysts microstructure. The extracted crystallite size was found to be
21   similar to the size observed for in situ reduction of the Cat-TPH catalyst.
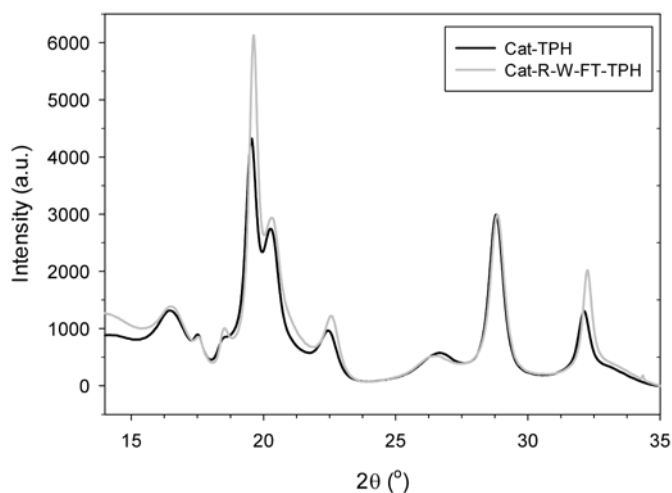
22
23   **Figure 8.** Comparison of XRPD patterns of the catalyst TPH treated in reduced state and TPH treated
24   after a month under FT synthesis.

25

26   Another important parameter that may affect interpretation of the XRPD patterns is
27   the polycrystalline nature of Co particles consisting of cobalt in hexagonal as well as cubic
28   configuration. The existence of the intergrown phases is explained by the formation of

stacking faults originating from the low activation energy of the sliding of Co atomic planes (Ea=14 kJ/mol per Co atom) [39]. The complete decomposition of the XRPD pattern into the two crystal structures requires detailed understanding of the stacking faults and/or other grain boundaries in the nanoparticle and the formation of a model that quantitatively reflects these structural defects. This delicate crystallographic refinement is outside the scope of this study and the observation of possible variations in the existence of the two phases has been made by monitoring changes in the normalised intensities of the observed reflections Table 3. Two basic conclusions can be drawn from the derived intensities. Initially, it is apparent that the intensities of the reference compounds are very different from the ones measured in the samples, a fact that supports the intergrown formation of the two phases. Secondly, the acquired normalised intensities for the Cat-TPH and Cat-R-W-FT-D-TPH show substantial similarities suggesting that there is not a major change in the ratio of the two phases during the progress of FT reaction. For the case of the (100) hcp-Co for which the biggest variation in the value is observed, it should be noted that elimination of the contribution from the overlapping (200) CoO reflection may explain the increased value.

Table 3

Normalised intensities of the reflections of fcc and hcp cobalt phases, found in the fresh and spent catalyst after TPH treatment, together with reference intensities of pure phases for comparison.

| Planes (hkl)	Reference hcp	fcc	Cat-TPH	Cat-R-W-FT-D-TPH
100	20	-	34	42
111	-	100	100	100
200	-	40	25	26
101	100	-	40	38
220	-	25	78	85

Although there is evidence for the stability of the co-existing crystalline phases, crystallite size analysis from XRPD is not conclusive since it tends to underestimate the crystallite size. Therefore, TEM was conducted to eliminate this uncertainty.

3.4. Transmission electron microscopy

TEM images of the passivated Cat-R-W-D and Cat-R-W-FT-D catalysts were obtained and are presented in Figure 9 and Figure 10. Figure 9a shows aggregates of Co nanoparticles on the alumina substrate. The dark areas are Co containing phases and bright areas are alumina. Co nanoparticles are distinctly observed in the aggregates, confirming that the sample has remained largely reduced. Figure 9b shows HRTEM images of a Co

1   nanoparticle. Fringes in the image show atomic spacing (d) that can be used to identify the

2   structure of the material. Fringes in the centre of the particle in Figure 9b, show the d value of

3   2.03 Å, confirming the presence of fcc-Co. However, fringes around the edges show a d

4   value of 1.94 corresponding to (101) hcp-Co. It is interesting to note that twins are observed

5   in the interface between Co and the alumina substrate, indicating the physical interaction

6   between the two.

7
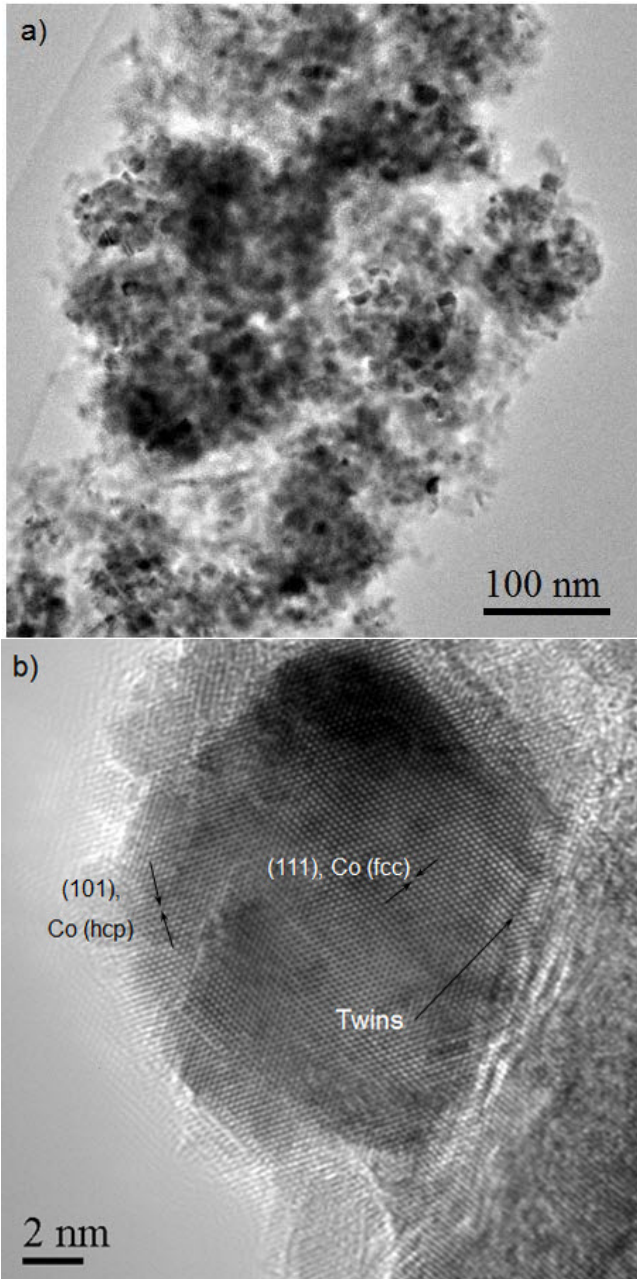
8
9   **Figure 9.** (a) TEM image of reduced-passivated Co-Re/γ-Al_2O_3 catalyst Cat-R-W-D, (b) HRTEM image

10 of cobalt nanoparticle.

11

12 Figure 10a shows the distribution of Co nanoparticles on the alumina substrate in the Cat-R-

13 W-FT-D catalyst. Most of the Co phases appear as separate particles. Figure 10b shows a

14 HRTEM image of a Co nanoparticle in the Cat-R-W-FT-D catalyst. Fringes in this image

show the d value of 1.94 Å which corresponds to (101) atomic plane in hcp-Co. HRTEM and diffraction were applied to define the Co-phase in the catalysts. HRTEM images confirmed that most of the Co-nanoparticles are in metallic state. A thin layer of CoO or Co_3O_4 was present at the surface of some of these nanoparticles, which can be formed during the de-waxing treatment or while the sample was transferred to the TEM. Confirming the HRTEM observations, the presence of weak diffraction from Co oxide phases were observed in the diffraction patterns from this catalyst.
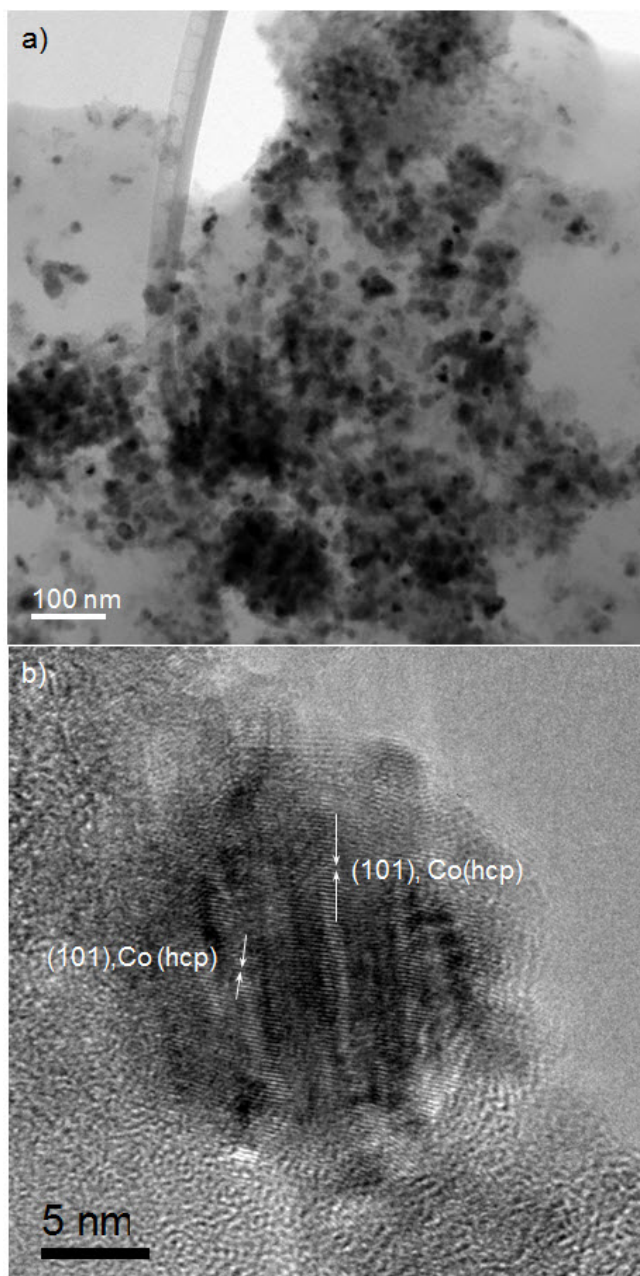
Figure 10. (a) TEM image of spent- passivated Co-Re/γ-Al₂O₃ Cat-R-W-FT-D, (b) HRTEM image of a cobalt nanoparticle.

1
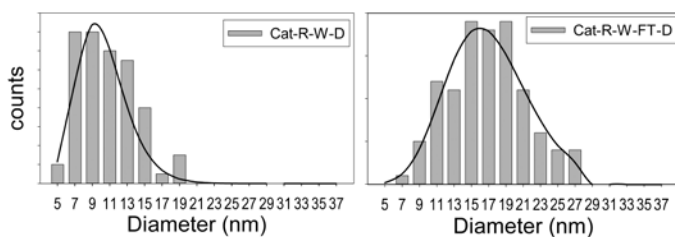
2 **Figure 11.** Histograms showing the particle size distribution from a sample of 100 particles as

3 measured in Cat-R-W-D and Cat-R-W-FT-D catalytic materials.

4

5 Cobalt particle size measurements were performed on TEM images similar to Figure 9a and

6 Figure 10a, from a sample of approximately 100 particles. Figure 11 shows the Co particle size

7 distribution in Cat-R-W-D and Cat-R-W-FT-D, respectively. The average Co particle size in

8 Cat-R-W-D material is 11.5±3.5 nm and for Cat-R-W-FT-D is 16.9±5.3 nm. Apart from the

9 change in the distribution of the Co particle size, the way that the Co nanoparticles are

10 dispersed on the γ-Al_2O_3 support appears to be different.

11   This can be better visualized in the dark field image (Figure 12) where the Cat-R-W-

12 FT-D catalyst, that has undergo FTS for a month in a slurry phase reactor, appears to have

13 less aggregated nanoparticles which are more scattered on the alumina support. This differs

14 from observations on fresh calcined catalysts made for FTS that exhibit a high degree of

15 aggregation [9,40].

200 nm

16
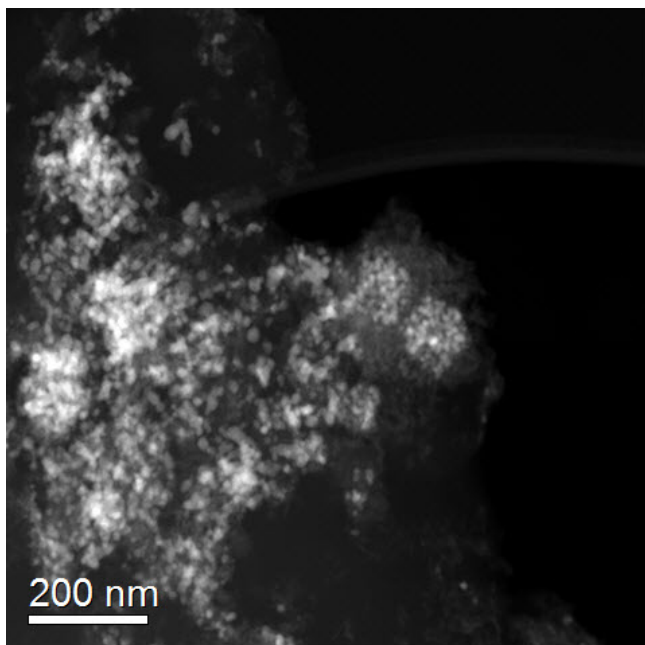
17 **Figure 12.** Dark field TEM image from spent catalyst. Cobalt nanoparticles appear as bright areas.

18

19 3.5. H_2 Chemisorption

20 H_2 chemisorption was performed on the reduced catalyst powder (Cat-TPH) and the spent

21 de-waxed catalyst (Cat-R-W-FT-D-TPH) after reduction. The two catalytic materials were

subjected to the same reduction protocol. The waiting time at set point temperature was increased to 10h in order to remove remaining hydrocarbons by hydrocracking [9,12]. An average size of the cobalt particles was calculated with the procedures previously proposed [17,41]. Results show that metal dispersion for the calcined catalyst after reduction reaches 7.6 % which can be translated to an average Co particle size of 12.6 nm. On the other hand, results on the spent catalyst show a significantly decreased dispersion of 2.9 % that is translated to a size of 32.9 nm. The chemisorption results suggest a substantial loss of active surface area which is not in agreement with the other two applied techniques. A possible reason for the observed discrepancy may be the existence of hard waxes or polymeric carbon that could not be removed by the applied low temperature hydrogenation treatment [12] rendering only part for the cobalt accessible to chemisorption.

Table 4: Summary of the particle or crystallite size in nanometres of cobalt obtained from various techniques.

Technique	Cat	Cat-TPH	Cat-R-W-D	Cat-R-W-FT-D	Cat-R-W-FT-D-TPH
H_2 chemisorption	-	12.6	-	-	32.9
-DOR corrected	-	9.1	-	-	26.3
XRPD	10.6[a] (13.2[b])	7.9	-	8.7	11.3
TEM	-	-	11.5	16.9	-

[a]Calculated according to Rønning et al. [37], [b]Co_3O_4 phase

4. Discussion

Results from the three most commonly applied size sensitive techniques are consistent with loss of Co surface area after a month of operation at commercial FTS conditions. This clearly demonstrates that sintering is one of the major deactivation mechanisms occurring during FTS in slurry bubble column reactors. An approximate increase of 43% and 47% can be calculated for the size of cobalt nanoparticles from XRPD and TEM, respectively. By assuming spherical cobalt nanoparticles, dispersion can be derived from the cobalt crystallite/particle size by the following equation: $D=96/d(Co^o)$ [17]. The sizes obtained by XRPD and TEM agree on an approximate loss in surface area equal to 30%. However, the loss of surface area cannot account for the entire observed activity decline [42] suggesting that other deactivation mechanisms co-exist. Attrition may lead to loss of catalyst material and has been detected in similar trials, it may therefore contribute to the observed loss of activity [43,44]. The present results are in good agreement with reports on $Co/Pt/Al_2O_3$ catalyst operated for 150 days at industrially relevant conditions in a 0.9 m diameter slurry bubble column pilot plant [9]. During the test, 40% of the total deactivation was attributed to sintering in addition to an observed further reduction of cobalt [45].

1   The phenomenon of sintering of supported metallic nanoparticles is greatly related to
2   the applied conditions and the properties of the catalytic material. In particular the rate of
3   sintering is influenced by temperature, chemical atmosphere, type of support, added
4   promoter, and metal particle size [46,47]. Low temperature FTS operates at temperatures
5   lower than the Hüttig and Tamman temperatures, at which either the atoms in defects or the
6   bulk atoms would have increased mobility, respectively. In addition, the catalysts are
7   exposed to high temperatures for several hours during their activation treatment prior to FT
8   reaction and can retain their size even at the scale of a few nanometres in diameter [48,49].
9   Thus, the applied conditions indicate that the observed sintering is highly unlikely to be
10   temperature induced. Besides, FTS environment in a slurry bubble column reactor is
11   governed by high partial pressures of H_2 and steam, in addition to CO, CO_2, and the
12   hydrocarbons produced. Steam is known to have an accelerating effect on the sintering rate
13   of supported metal nanoparticles under reducing atmospheres [46]. This has been
14   documented for nickel based catalysts used in steam reforming and methanation reactions,
15   although at significantly higher temperatures than FTS conditions [50,51]. Common
16   interpretation of the acceleration of the sintering phenomenon under high partial pressures of
17   steam is the mobility enhancement that adsorbed hydroxyl groups may induce [52].
18   Experimental results under model conditions agree with density functional theory (DFT) that,
19   in the case of Ni, such behaviour can be attributed to the formation of -OH metal dimers that
20   can easily form (ΔE = 58 kJ mol^{-1}) at steam environment and thereby increase diffusivity of
21   atoms or nanoparticles.

22   A similar hypothesis for sintering enhancement of hydrated Co nanoparticles has
23   been made by researchers at Shell, where TEM and Mössbauer spectroscopic techniques
24   were applied to model catalytic systems of Co supported on carbon materials model
25   conditions. A correlation between the H_2O/H_2 ratio and the degree of sintering was observed.
26   Authors suggested the formation of cobalt hydroxyl groups as an initiation step that allowed
27   the movement of Co particles on the wetted support [53]. In a different perspective, a two-
28   step mechanism that proposes diffusion of Co particles initiated by re-oxidation of the Co
29   surface by steam has been reported [10,54–56]. According to the authors, the cobalt oxide
30   formed further wets the support, eventually resulting in the coalescence of the Co particles.
31   However, this hypothesis is contradictory with the tendency of cationic cobalt to react with
32   the γ-Al_2O_3 support and enter into lattice forming metal aluminates, [57] thereby increasing
33   metal-support interaction and consequently impede metal diffusion. In addition oxide species
34   are stabilizing Co nanoparticles by decreasing their surface energy [58] and thus minimize
35   driving forces that lead to sintering [59].

36   From the above it appears that sintering is induced by the FT environment and that
37   either hydroxyl or oxide species may initiate the phenomenon. Naturally, the next question at

hand is on the way that Co particles grow. Sintering of metallic nanoparticles can occur through three principal mechanisms, crystallite migration and eventually coalescence, atomic migration (Ostwald-ripening) and vapour transport [60]. Vapour transfer may be excluded due to the fact that low temperatures are used and no significant formation of Co carbonyls (at least in the short term experiments discussed here) is observed [61].

So far, particle migration, collision and eventual coalescence are frequently postulated as the sintering mechanisms for FTS. In particular, Bezemer et al. [62] suggested coalescence as the prevailing mechanism due to TEM observations of the close proximity that Co nanoparticles are found on the spent catalyst. Sadeqzadeh et al. [54] proposed particle migration and coalescence after comparing models using generalized power law expressions (GPLE) of first and second-order, that were applied on in situ XRPD derived experimental data. It has been anticipated that the coalescence mechanism can be fitted by a second-order GPLE model, while a first order fit denotes an Ostwald ripening type of mechanism [46]. Coalescence of Co nanoparticles supported on γ-Al_2O_3 has been suggested to take place at thermal treatments and reducing environments. Lok has used TEM-PSD to understand sintering occurring during reduction of highly dispersed Co catalysts [63]. Coalescence was the speculated mechanism of particle growth during reduction. Fundamental studies on Co nanoparticle coalescence upon thermal treatments have been described previously in model systems monitored by in situ TEM [64].

Here, the shape of particle size distributions (PSD) obtained from TEM (Figure 11) and features existing in the PSD histograms have been used to assist in the understanding of sintering mechanisms [65]. Such an approach for deduction of sintering mechanisms has for long been debated [66]. Although it appears that the shape of the PSD is strongly related to several parameters (i.e. the shape of the initial PSD, the time on stream of the sampling), the method alone is not conclusive, but a good indication of the growth mechanism can be extracted. A similar approach has been used on Ni/γ-Al_2O_3 catalysts for steam reforming [67], where a condition dependence of the sintering mechanism also was demonstrated [51].

If the PSD based approach is applied to the results obtained by TEM in the present work, it appears that sintering is likely to be through crystallite migration. This outcome arises from two main features of the TEM histograms. In particular, the existence of a tail on the large diameter side in addition to the absence of sharp cut-off and tail on the low diameter side are indications of a liquid-like coalescence mechanism. This PSD can be adequately fitted by a long-normal distribution model. Furthermore, catalysts produced on industrial scale often have less defined structure with higher degree of heterogeneity. In the case of cobalt incipient wetness impregnation on high surface area γ-Al_2O_3 supports, this method regularly leads to nanoparticles in large agglomerates [9,40]. HRTEM images show that the Co aggregate formation commonly found on fresh catalysts [40,68], although it still exists, is

less pronounced after a month of operation on stream and several cobalt nanoparticles are distributed distinctly in the alumina substrate. This observation supports the idea that Co nanoparticles are mobile under FTS-operation. In the Ostwald ripening process atoms or atomic species diffuse on the support and are captured by larger immobile nanoparticles. In that sense Co nanoparticles are expected to maintain their positions [66] and consequently keep their aggregated environment while the nanoparticles grow in size. From the present TEM observations it is evident that nanoparticles are not maintaining their position, a fact that is strengthening the particle migration postulation.

Regarding modelling of the sintering deactivation process, even if the correct mechanism is chosen, deviations should be expected with the current state of knowledge due to several secondary parameters of Co supported catalysts that still have not been clarified. In particular, Co nanoparticles are, as commonly visualised by in situ XRD, composed by two intergrown crystalline phases (fcc and hcp) with a high population of stacking faults [38,69,70]. The contribution of the stacking faults and possible strain in the surface energy of the nanoparticles on catalytic behaviour is not yet understood. Towards the optimization of catalyst performance, cobalt nanoparticles designed for industrial FTS application are ideally prepared in sizes between 8-10 nm for the optimum activity and selectivity that these sizes offer [8,9,48,49]. From the calculated particle size distribution of the present catalyst, it appears that 18% of the cobalt particles in the fresh catalyst have an average diameter of 5-8 nm, falling in the range in which structure sensitivity may play a role [48] for the observed catalytic behaviour. In addition, in situ cobalt reduction will also play a role. Thus, a positive effect of particle growth on catalyst activity counteracting deactivation processes should not be underestimated. Finally, in relation to the previously mentioned structure sensitivity and its connection to the reaction mechanism, the model may have to be tuned to describe the change in the population of specific sites that are proposed to be the active assembles catalysing C-C coupling. These can be either Co surface planes [71,72] or sites found in stepped surfaces e.g. the Co (211) stepped surface (known as B5 sites) [73]. Therefore models are expected to deviate from the deactivation curve if the pre-mentioned parameters are not addressed.

From the present data, any effect of rhenium on the overall deactivation profile cannot be extracted since the X-ray absorption spectra on the Re L_{III} edge appear rather similar having characteristics from oxide and metallic states. However, it is obvious that rhenium does not experience severe changes during the course of the reaction at a realistic FTS environment. The moderate signal-to-noise ratio, due to low concentrations, together with the uncertainty that derives from the ex situ nature of the current experiments could be overcome by in situ investigations where relative changes are targeted [33].

1   In the present study, the Co-Re/γ-Al$_2$O$_3$ catalyst is initially stable against sintering

2   since Co particle sizes in the starting material are large enough to have only a moderate

3   tendency towards growth. The high surface area of the support is also expected to retard

4   sintering. In addition to the classical approach of stabilization of nanoparticles by varying the

5   catalyst support or addition of promoters, the importance of parameters such as the ideal

6   spacing between metal nanoparticles and the particle size distribution were also recently

7   demonstrated [74,75]. It is becoming evident that not only the individual particle properties

8   should be targeted but the collective properties of the Co particles present in the alumina

9   frame. There are room for improvement since even if the collective properties are optimized

10   towards stability against sintering they may negatively interfere with selectivity [76].

11   It is well documented that the degree of reduction/reducibility of Co-based catalysts

12   supported on γ-Al$_2$O$_3$ is a function of particle size, metal loading [77] and promoter [78]. The

13   higher degree of reduction measured in the spent catalyst could be explained through the

14   observed larger cobalt particle size resulting in reduced metal-support interaction allowing

15   further reduction to occur. It follows that the FT environment is reducing and not oxidising,

16   despite the high partial pressure of steam that would suggest otherwise. The simultaneous

17   observation of sintering and further reduction has been detected by several authors in the

18   past, visualised either in situ [23,37,62,79] or ex situ [5,45]. Our ex situ measurements on

19   wax protected catalysts, either freshly reduced and embedded in wax or spent, also point to

20   re-oxidation having occurred during storage or de-waxing. Therefore, purely ex situ results

21   should be processed with care in terms of degree of reduction and/or crystallite size analysis.

22   The recent advantages in the in situ characterisation of catalytic materials under

23   reactive environments provide a powerful tool for better understanding of the behaviour of

24   nanoparticles under realistic conditions. In FTS, sintering appears to play a major role in the

25   deactivation observed during the first month on stream. However, mechanistic understanding

26   is still missing and, ideally, in situ studies of XRPD and ASAXS as well as direct observations

27   by environmental TEM (ETEM) on well-defined model materials imitating commercial

28   catalysts that are examined under relevant conditions in combination with modelling will give

29   insight on the exact sintering mechanisms.

30

31   **5. Conclusions**

32   Ex situ and quasi-in situ characterization of calcined, reduced and spent Co-Re/γ-Al$_2$O$_3$

33   catalysts used in a semi-commercial scale FTS unit was performed. Results from XRPD and

34   TEM have shown that cobalt particles are losing approximately 30% of their surface area

35   during the evolution of the reaction. In addition, both the X-ray based techniques agree that

36   the spent catalyst exhibits higher reducibility. A minor content of cobalt–aluminates was

37   detected by Co-XANES. It appears also that Re is in a partially reduced state in both

catalysts before and after reaction. Finally, indications of a prevailing particle migration mechanism instead of Oswald ripening were extracted from the TEM images.

References

[1] T. Remans, G. Jenzer, A. Hoek, in:, G. Ertl, H. Knözinger, F. Schüth, Jens Weitkamp (Eds.), Handb. Heterog. Catal., Wiley-VCH Verlag GmbH & Co. KGaA, Weinheim, Germany, 2008, pp. 2994–3010.

[2] E. Salehi, W. Nel, S. Save, Hydrocarb. Process. (2013) 41–48.

[3] M.E. Dry, Catal. Today 71 (2002) 227–241.

[4] N.E. Tsakoumis, M. Rønning, Ø. Borg, E. Rytter, A. Holmen, Catal. Today 154 (2010) 162–182.

[5] A.M. Saib, D.J.D.J. Moodley, I.M.I.M. Ciobîcă, M.M. Hauman, B.H. Sigwebela, C.J. Weststrate, J.W.W. Niemantsverdriet, J. van de Loosdrecht, Catal. Today 154 (2010) 271–282.

[6] P.J. van Berge, R. Everson, Stud. Surf. Sci. Catal. 107 (1997) 207–212.

[7] J.L. Casci, C.M. Lok, M.D. Shannon, Catal. Today 145 (2009) 38–44.

[8] D. Ozkaya, C.M. Lok, J. Casci, P. Ash, in:, S. Richter, A. Schwedt (Eds.), 14th Eur. Microsc. Congr., Springer Berlin Heidelberg, Berlin, Heidelberg, 2008, pp. 249–250.

[9] M.J. Overett, B. Breedt, E. du Plessis, W. Erasmus, J. van de Loosdrecht, Prepr. - Am. Chem. Soc. Div. Pet. Chem. 53 (2008) 126–128.

[10] G. Kiss, C.E. Kliewer, G.J. Demartin, C. Culross, J.E. Baumgartner, J. Catal. 217 (2003) 127–140.

[11] G. Jacobs, Y. Zhang, T.K. Das, J. Li, P.M. Patterson, B.H. Davis, Stud. Surf. Sci. Catal. 139 (2001) 415–422.

[12] D.J. Moodley, J. van de Loosdrecht, A.M. Saib, M.J. Overett, A. Datye, J.W. Niemantsverdriet, Appl. Catal. A Gen. 354 (2009) 102–110.

[13] J.J.H.M.F. Freide, T.D. Gamlin, J.R. Hensman, B. Nay, C. Sharp, J. Nat. Gas Chem. 13 (2004) 1–9.

[14] S.-J. Park, J.W. Bae, Y.-J. Lee, K.-S. Ha, K.-W. Jun, P. Karandikar, Catal. Commun. 12 (2011) 539–543.

[15] L. Pinard, P. Bichon, A. Popov, J.L. Lemberton, C. Canaff, F. Maugé, P. Bazin, E.F. S.-Aguiar, P. Magnoux, Appl. Catal. A Gen. 406 (2011) 73–80.

[16] P. Taylor, D. Schanke, M. Wagner, Hydrocarb. Eng. (2008) 37–42.

[17] R. Reuel, C.H. Bartholomew, J. Catal. 77 (1984) 63–77.

[18] W. van Beek, O. V. Safonova, G. Wiker, H. Emerich, Phase Transitions 84 (2011) 726–732.

1 [19] B. Ravel, M. Newville, J. Synchrotron Radiat. 12 (2005) 537–41.

2 [20] J.W. Couves, J.M. Thomas, D. Waller, R.H. Jones, A.J. Dent, G.E. Derbyshire, G.N.
3 Greaves, Nature 354 (1991) 465–468.

4 [21] B.S. Clausen, G. Steffensen, B. Fabius, J. Villadsen, R. Feidenhans'l, H. Topsøe, J.
5 Catal. 132 (1991) 524–535.

6 [22] N.E. Tsakoumis, A. Voronov, M. Rønning, W. van Beek, Ø. Borg, E. Rytter, A.
7 Holmen, J. Catal. 291 (2012) 138–148.

8 [23] N.E. Tsakoumis, R. Dehghan, R.E. Johnsen, A. Voronov, W. van Beek, J.C.
9 Walmsley, Ø. Borg, E. Rytter, D. Chen, M. Rønning, A. Holmen, Catal. Today 205
10 (2013) 86–93.

11 [24] P. Norby, J. Appl. Crystallogr. (1997) 21–30.

12 [25] A. Hammersley, S. Svensson, M. Hanfland, A. Fitch, D. Hausermann, High Press.
13 Res. 14 (1996) 235–248.

14 [26] M. Wojdyr, J. Appl. Crystallogr. 43 (2010) 1126–1128.

15 [27] A. Coelho, (2008) Topas V4.2 (Bruker AXS), Karlsruhe, Germany.

16 [28] P. Norby, J. Am. Chem. Soc. 119 (1997) 5215–5221.

17 [29] D.S. Wragg, F.L. Bleken, M.G. O'Brien, M. Di Michiel, H. Fjellvåg, U. Olsbye, Phys.
18 Chem. Chem. Phys. 15 (2013) 8662–71.

19 [30] D.J. Moodley, A.M. Saib, J. van de Loosdrecht, C.A. Welker-Nieuwoudt, B.H.
20 Sigwebela, J.W. Niemantsverdriet, Catal. Today 171 (2011) 192–200.

21 [31] F. Huber, Z. Yu, S. Lögdberg, M. Rønning, D. Chen, H. Venvik, A. Holmen, Catal.
22 Letters 110 (2006) 211–220.

23 [32] J. Wong, F. Lytle, R. Messmer, D. Maylotte, Phys. Rev. B 30 (1984).

24 [33] A. Voronov, N.E. Tsakoumis, N. Hammer, W. van Beek, H. Emerich, M. Rønning,
25 Catal. Today (2014) in press DOI:10.1016/j.cattod.2013.11.069.

26 [34] S.R. Bare, S.D. Kelly, F. D.Vila, E. Boldingh, E. Karapetrova, J. Kas, G.E. Mickelson,
27 F.S. Modica, N. Yang, J.J. Rehr, J. Phys. Chem. C 115 (2011) 5740–5755.

28 [35] A.S. Fung, P.A. Tooley, M.J. Kelley, D.C. Koningsberger, B.C. Gates, J. Phys. Chem.
29 95 (1991) 225–234.

30 [36] R.J. Lobo-Lapidus, B.C. Gates, J. Catal. 268 (2009) 89–99.

31 [37] M. Rønning, N.E. Tsakoumis, A. Voronov, R.E. Johnsen, P. Norby, W. van Beek, Ø.
32 Borg, E. Rytter, A. Holmen, Catal. Today 155 (2010) 289–295.

33 [38] O. Ducreux, B. Rebours, J. Lynch, D. Bazin, M. Roy-Auberger, Oil Gas Sci. Technol. -
34 Rev. l'IFP 64 (2008) 49–62.

1   [39]   A.M. Saib, A. Borgna, J. van de Loosdrecht, P. Van Berge, J.W. Geus, J.W.
2   Niemantsverdriet, J. Catal. 239 (2006) 326–339.

3   [40]   I. Arslan, J.C. Walmsley, E. Rytter, E. Bergene, P.A. Midgley, J. Am. Chem. Soc. 130
4   (2008) 5716–5719.

5   [41]   R. Jones, C.H. Bartholomew, Appl. Catal. 39 (1988) 77–88.

6   [42]   E. Rytter, S. Eri, T.H. Skagseth, Ø. Borg, Fischer-Tropsch Catalyst Regeneration, US
7   20130210939A1, 2013.

8   [43]   D. Schanke, M. Wagner, P. Taylor, in:, Proc. 1st Annu. Gas Process. Symp. 10–12
9   January 2009, Doha, Qatar, First Edit, Elsevier B.V., 2009, pp. 370–377.

10   [44]   Statoil ASA, Gas-to-Liquids (GTL) Technology, 2006.

11   [45]   J. van de Loosdrecht, B. Balzhinimaev, J.-A. Dalmon, J.W. Niemantsverdriet, S.V.
12   Tsybulya, A.M. Saib, P.J. van Berge, J.L. Visagie, J. van de Loosdrecht, P.J. van
13   Berge, Catal. Today 123 (2007) 293–302.

14   [46]   C.H. Bartholomew, Appl. Catal. A Gen. 107 (1993) 1–57.

15   [47]   C.T. Campbell, S.C. Parker, D.E. Starr, Science 298 (2002) 811–4.

16   [48]   G.L.L. Bezemer, J.H. Bitter, H.P.C.E. Kuipers, H. Oosterbeek, J.E. Holewijn, X. Xu, F.
17   Kapteijn, A.J. van Dillen, K.P. de Jong, J. Am. Chem. Soc. 128 (2006) 3956–3964.

18   [49]   Ø. Borg, P.D.C. Dietzel, A.I. Spjelkavik, E.Z. Tveten, J.C. Walmsley, S. Diplas, S. Eri,
19   A. Holmen, E. Rytter, J. Catal. 259 (2008) 161–164.

20   [50]   C.H. Bartholomew, R.R.B. Pannell, R.W.R. Fowler, J. Catal. 79 (1983) 34–46.

21   [51]   J. Sehested, J.A.P. Gelten, I.N. Remediakis, H. Bengaar, J.K. Nørskov, J. Catal. 223
22   (2004) 432–443.

23   [52]   M.A. Martín, J.A. Pajares, L. González Tejuca, J. Colloid Interface Sci. 107 (1985)
24   540–546.

25   [53]   G.L.L. Bezemer, T.J. Remans, A.P. van Bavel, A.I.I. Dugulan, J. Am. Chem. Soc. 132
26   (2010) 8540–1.

27   [54]   M. Sadeqzadeh, J. Hong, P. Fongarland, D. Curulla-Ferré, F. Luck, J. Bousquet, D.
28   Schweich, A.Y. Khodakov, Ind. Eng. Chem. Res. 51 (2012) 11955–11964.

29   [55]   M. Sadeqzadeh, S. Chambrey, S. Piché, P. Fongarland, F. Luck, D. Curulla-Ferré,
30   Catal. Today 215 (2013) 52–59.

31   [56]   C. Kliewer, G. Kiss, S. Soled, Microsc. Microanal. 16 (2010) 1258–1259.

32   [57]   P.H. Bolt, F.H.P.M.. Habraken, J.W. Geus, J. Solid State Chem. 135 (1998) 59–69.

33   [58]   E. van Steen, M. Claeys, M.E. Dry, J. van de Loosdrecht, E.L. Viljoen, J.L. Visagie, J.
34   Phys. Chem. B 109 (2005) 3575–7.

[59] B.I. Chorkendorff, J.W. Niemantsverdriet, Concepts of Modern Catalysis and Kinetics, WILEY-VCH Verlag GmbH & Co. KGaA, 2003.

[60] C.H. Bartholomew, Appl. Catal. A Gen. 212 (2001) 17–60.

[61] E. van Steen, M. Claeys, Chem. Eng. Technol. 31 (2008) 655–666.

[62] G.L.L. Bezemer, T.J. Remans, A.P. van Bavel, A.I.I. Dugulan, J. Am. Chem. Soc. 132 (2010) 8540–1.

[63] C. Lok, Stud. Surf. Sci. Catal. (2004) 283.

[64] G. Palasantzas, T. Vystavel, S.A. Koch, J.T.M. De Hosson, Mater. Sci. (2006) 2–6.

[65] C.G. Granqvist, R.A. Buhrman, J. Catal. 42 (1976) 477–479.

[66] S.R. Challa, A.T. Delariva, T.W. Hansen, S. Helveg, J. Sehested, P.L. Hansen, F. Garzon, A.K. Datye, J. Am. Chem. Soc. 133 (2011) 20672–5.

[67] J. Sehested, A. Carlsson, T.V.W. Janssens, P.L. Hansen, A.K. Datye, J. Catal. 197 (2001) 200–209.

[68] R. Dehghan, T.W. Hansen, J.B. Wagner, A. Holmen, E. Rytter, Ø. Borg, J.C. Walmsley, Catal. Letters 141 (2011) 754–761.

[69] R. Srinivasan, R.J. De Angelis, P.J. Reucroft, A.G. Dhere, J. Bentley, J. Catal. 116 (1989) 144–163.

[70] L.J.E. Hofer, W. Peebles, J. Am. Chem. Soc. (1947) 2497–500.

[71] S. Storsæter, D. Chen, A. Holmen, Surf. Sci. 600 (2006) 2051–2063.

[72] M. Ojeda, R. Nabar, A.U. Nilekar, A. Ishikawa, M. Mavrikakis, E. Iglesia, J. Catal. 272 (2010) 287–297.

[73] R.A. van Santen, I.M. Ciobîcă, E. van Steen, M.M. Ghouri, Adv. Catal. 54 (2011) 127–187.

[74] G. Prieto, J. Zečević, H. Friedrich, K.P. de Jong, P.E. de Jongh, Nat. Mater. 12 (2013) 34–9.

[75] L.A. Richard, P. Moreau, S. Rugmini, F. Daly, Appl. Catal. A, Gen. 464-465 (2013) 200–206.

[76] T.M. Eggenhuisen, P. Munnik, H. Talsma, P.E. de Jongh, K.P. de Jong, J. Catal. 297 (2013) 306–313.

[77] W.J. Wang, Y.W. Chen, Appl. Catal. 77 (1991) 223–233.

[78] Ø. Borg, N. Hammer, S. Eri, O.A. Lindvåg, R. Myrstad, E.A. Blekkan, M. Rønning, E. Rytter, A. Holmen, Catal. Today 142 (2009) 70–77.

[79] M. Claeys, E. van Steen, J.L. Visagie, J. van de Loosdrecht, E. van Steen, K. Visagie, in:, 22nd North Am. Catal. Soc. Meet. June 5-10, Detroit, USA, 2007, p. 2007.